CHAPTER III
SOLUTION PROCEDURE

In this chapter, we summarize a numerical technique utilized to solve the boundary value problem associated with a cracked body, the post-process to extract the stress intensity factor from the data along the crack front, a meshing procedure for the CT specimen, and the mesh refinement and study of convergence of numerical solutions.

3.1 Weakly singular SGBEM

To solve the boundary value problem for a cracked body governed by a set of integral equations (2.22), a weakly singular SGBEM developed by Li *et al.* (1998) for cracks in isotropic media and by Rungamornrat and Mear (2008b) for cracks in generally anisotropic media is adopted. Due to the weakly singular nature of the governing integral equations and the symmetry of the formulation, this numerical technique is superior to other standard boundary integral equation methods in several aspects. For instance, C^0 interpolation functions can be used in the discretization of all boundary data, all singular integrals exist in an ordinary sense and can be integrated accurately and efficiently using some standard quadrature, and it finally results in a symmetric system of linear algebraic equations. It should be remarked also that the discretization is required only on the boundary of the domain and the crack surface and this renders the reduction of the spatial dimension from 3 to 2 for three-dimensional problems. Unlike the standard finite element method (e.g. Hughes, 2000), the discretization is required for the entire domain and the meshing effort is non-trivial especially in the region near the crack front where an extremely fine mesh is required to accurately capture the singularity of the stress field (e.g. Swenson and Ingraffea, 1988; Martha *et al.*, 1993; Ayhan *et al.*, 2003). For the SGBEM developed by Li *et al.* (1998) and Rungamornrat and Mear (2008b), the asymptotic behavior of the field near the crack front as discussed in sections 2.1 and 2.2 is directly and properly integrated into

the near front approximation allowing relatively coarse meshes be employed to construct reasonably accurate numerical results. Here, we only summarize some important aspects of the SGBEM adopted in the present study while details of the development can be found in the work of Li *et al.* (1998) and Rungamornrat and Mear (2008b).

3.1.1 Discretization

The unknown displacement and traction on the regular boundary of the domain are approximated by using continuous interpolation functions defined in an element-wise fashion on standard, two-dimensional, isoparametric, C^0 elements (e.g. Hughes, 2000) resulting from the discretization. The relative crack-face displacement along the crack front is approximated by special continuous interpolation functions via the use of special crack-tip elements developed by Li *et al.* (1998) and Rungamornrat and Mear (2008b). The relative crack-face displacement on the remaining of the crack surface is approximated by the interpolation functions from standard, two-dimensional, isoparametric, C^0 elements. It should be noted that for the CT specimen considered in this study, the crack front intersects the regular boundary at two particular points known as vertices. Since shape functions on the crack-tip elements and on the standard elements are different, an element on the regular boundary which contains the vertex and is adjacent to the crack-tip element must be modified to maintain the continuity of the displacement field. This can be achieved by using a special element developed by Li *et al.* (1998).

3.1.2 Evaluation of kernels

For an isotropic case, all four kernels $H_{ij}^{p}(\boldsymbol{\xi}-\mathbf{y})$, $U_{i}^{p}(\boldsymbol{\xi}-\mathbf{y})$, $G_{mj}^{p}(\boldsymbol{\xi}-\mathbf{y})$ and $C_{mj}^{tk}(\boldsymbol{\xi}-\mathbf{y})$ are given in an explicit form in terms of fundamental functions. Thus, evaluation of these kernels for every pair of source and field points $(\boldsymbol{\xi},\mathbf{y})$ is trivial. For the case of generally anisotropic materials, the kernel $H_{ij}^{p}(\boldsymbol{\xi}-\mathbf{y})$ can still be directly calculated while the evaluation of the kernels $U_{i}^{p}(\boldsymbol{\xi}-\mathbf{y})$, $G_{mj}^{p}(\boldsymbol{\xi}-\mathbf{y})$ and $C_{mj}^{tk}(\boldsymbol{\xi}-\mathbf{y})$ by directly integrating the closed contour integral (2.18) for every pair $(\boldsymbol{\xi},\mathbf{y})$ can lead to massive computational cost. In this study, the interpolation technique proposed by Rungamornrat and Mear (2008b) is utilized to avoid such direct integration.

3.1.3 Numerical integration

All regular, single surface integrals are accurately and efficiently integrated by using standard Gaussian quadrature. For double surface integrals, three types of integrals including regular integrals, singular integrals and nearly singular integrals are encountered after the discretization. All regular integrals can be efficiently evaluated using standard Gaussian quadrature while both singular and nearly singular integrals are integrated numerically using special quadratures developed by Xiao (1998). Positive features of those special quadratures are that the integration can be performed in the computational domain (i.e. master element), the singularity and rapid variation behavior are removed via using proper variable transformations, and the accuracy of the scheme finally controlled by adjusting the number of Gauss points.

3.1.4 Solution of system of linear equations

A final system of linear algebraic equations resulting from the discretization is symmetric and also positive definite for pure traction boundary value problems as considered in the present study. It is worth noting that proper constraints must be introduced in order to eliminate the rigid body translations and rigid body rotations or, equivalently, to ensure that the system of linear equations possesses a unique solution. For three-dimensional, pure traction boundary value problems, six constraints are needed. To solve such a symmetric, positive definite system of linear equations, a standard conjugate gradient method with Jacobi-preconditioning is utilized (e.g. Hamming, 1987; Chapra and Canale, 1990). The obtained solution (for pure traction boundary value problems) contains nodal displacements on the regular boundary, nodal relative crack-face displacements on the crack surface, and extra degrees of freedom along the crack front resulting from the use of crack-tip elements. The last quantities are associated with the gradient of the relative crack-face displacement along the crack front and they can be used in the determination of the stress intensity factors as discussed in the following section.

3.2 Determination of stress intensity factors

It is apparent that a solution obtained directly from the weakly singular SGBEM contains nodal quantities (displacements, tractions, and relative crack-face

displacement) on the regular boundary and the crack surface. The elastic field within the body (e.g. stress and displacement) can also be computed using the integral relations proposed by Rungamornrat and Mear (2008a). If only the stress intensity factors are of interest, the definition (2.8) offers a better candidate comparing to the definition in terms of the stress (2.5)-(2.7) in order to avoid the computation of the field within the body. It is noted however that the direct use of the definition (2.8) still requires the evaluation of the limit and this calculation may affect the accuracy of the stress intensity factors. To enhance the accuracy, Rungamornrat and Mear (2008b) employed a special feature of the crack-tip element along with (2.8) to develop an explicit, limit-free formula for determining the mixed-mode stress intensity factors as follows

$$k_i(\mathbf{x}_c) = \sqrt{\frac{\pi}{2J\sin\beta}} B_{il}(\mathbf{x}_c) \sum_{n=1}^{N} u^e_{l(n)} \psi_{(n)}(\mathbf{x}_c) \tag{3.1}$$

where $\mathbf{x}_c$ is any point on the crack front; J and β are parameters depending on the geometry of the crack-tip element at point $\mathbf{x}_c$ (see more details in the work of Rungamornrat and Mear, 2008b); N denotes the number of nodes in the crack-tip element; $u^e_{l(n)}$ is the nodal degree of freedom associated with the n^{th} node; and $\psi_{(n)}(\mathbf{x}_c)$ is the value of the nodal shape function at point $\mathbf{x}_c$. It is worth noting that $\psi_{(n)}(\mathbf{x}_c)$ is zero for all shape functions associated with nodes not located on the crack front; as a result, the summation appearing in the expression (3.1) involves only extra nodal degrees of freedom along the crack front. In addition, components of all quantities in the formula (3.1) are referring to the local coordinate system defined in section 2.1.

By using the crack-tip elements to approximate the relative crack-face displacement near the crack front along with applying the explicit formula (3.1) in the determination of the stress intensity factors, Rungamornrat and Mear (2008b) found that highly accurate results can be obtained by using only relatively coarse meshes. With such attractive feature, the formula (3.1) is therefore utilized in the present study.

3.3 Geometries of CT specimen

In the present study, we focus only on a particular cracked body with its configuration similar to a compact tension (CT) testing specimen. ASTM E399-90 (1997)

has recommended the geometries of the CT specimen in the experiment for the plane strain fracture toughness K_{IC} as shown in Figure 3.1. The ratio between the crack length a (measured from the center of each hole to the crack front) and the specimen width W (measured from the center of each hole to the back face of the specimen) must be chosen in the range of 0.45 to 0.55 and the thickness is recommended to be $0.5W$. The entire width (measured from the back face to the front face) is equal to $1.25W$. A pair of equal and opposite loads is to be applied at the holes of radius $0.25W$ to open the crack. The distance between the center of each hole and the crack plane is equal to $0.275W$ and the distance from the crack plane to the top and bottom surface of the specimen is equal to $0.6W$. Details of a small starter notch in front of the crack plane can be found in ASTM E399-90 (1997).

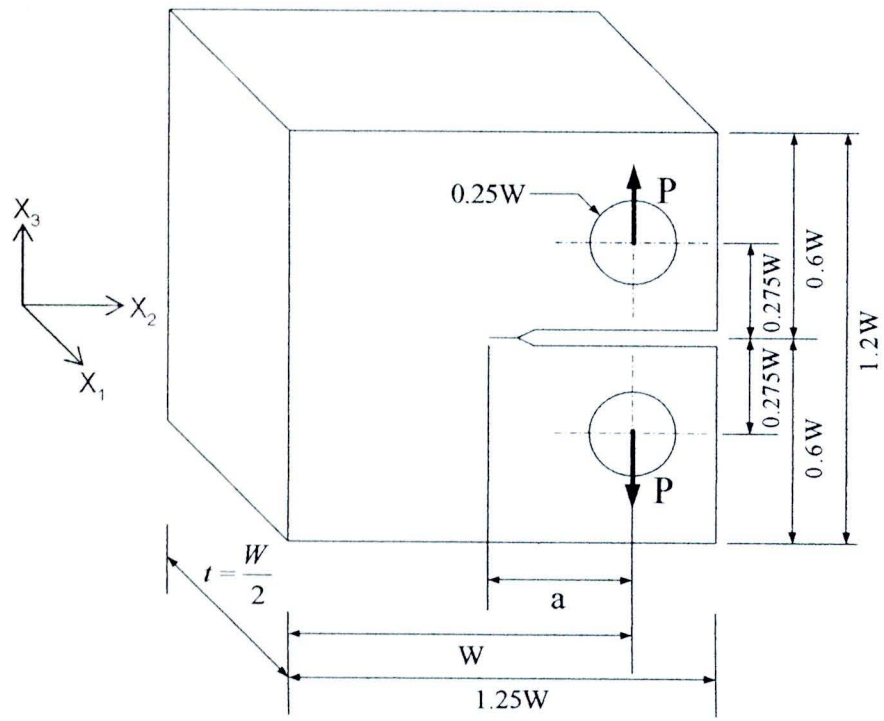

Figure 3.1 Configuration of compact tension (CT) specimen recommended by ASTM E399-90 (1997)

In the modeling, we choose a configuration as shown in Figure 3.2 to represent the CT specimen shown in Figure 3.1. The difference between this model and the actual CT specimen is due to the removal of the notch and then replacing it by a

through-the-thickness crack. It is worth noting that this simplification should not significantly alter the behavior of the problem but substantially reduces the meshing effort. In the analysis, we choose $a/W = 0.5$ and the thickness of the specimen is varied in order to investigate its influence on the distribution of the stress intensity factor. The applied loads at both holes are assumed to be uniformly distributed over the upper part of the upper hole and the lower part of the hole.

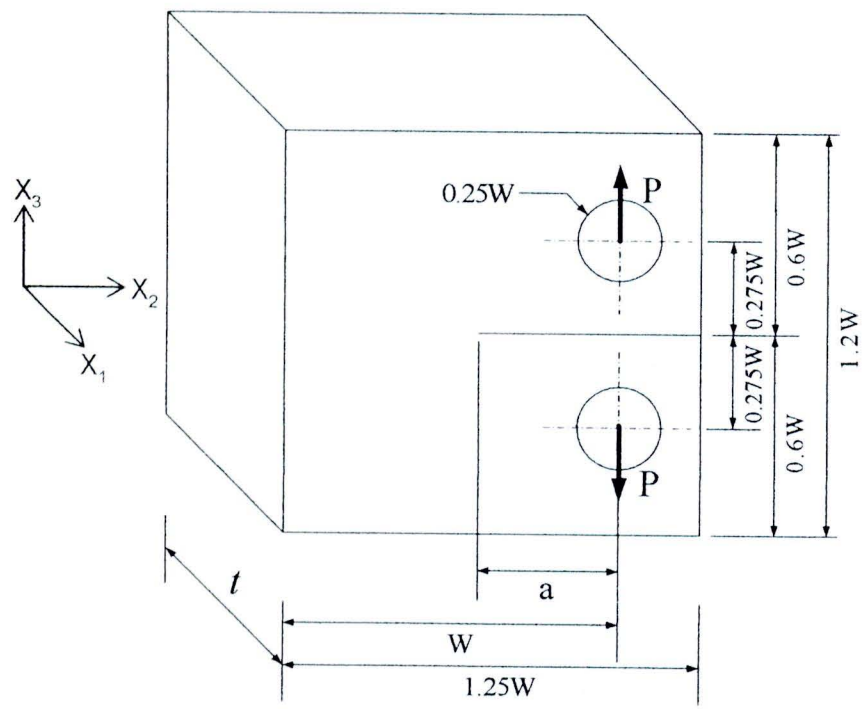

Figure 3.2 Configuration of compact tension (CT) specimen used in the analysis

3.4 Mesh generation

In the construction of a finite element mesh on the boundary of the CT specimen and the crack surface, the number of distorted elements and elements with a large aspect ratio is minimized, a finer mess is utilized in regions where fields are anticipated to be complex such as regions near the crack front and vertices, and a mesh with smooth transition is employed to connect the fine mesh region and the coarse mesh region. Three types of elements are utilized in the discretization of the CT specimen: (i) standard 6-node triangular elements and standard 8-node quadrilateral

elements shown in Figure 3.3(a)-(b), (ii) 9-node quadrilateral crack-tip elements shown in Figure 3.3(c), and (iii) special 9-node quadrilateral elements shown in Figure 3.3(d). More specifically, elements in the second category are utilized only along the entire crack front whereas on the front and back faces of the specimen, two elements of the last type must be used to connect the crack-tip element and the standard elements. The remaining boundary and crack surface are discretized by elements in the first category.

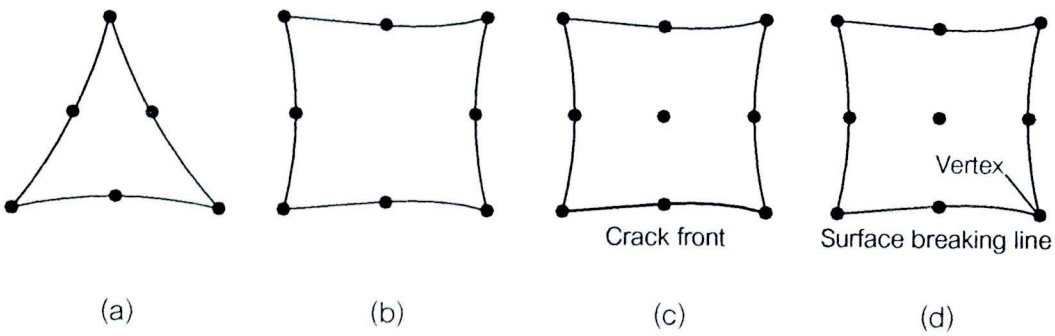

Figure 3.3 Schematic of elements utilized in the discretization of CT specimen: (a) standard 6-node triangular element, (b) standard 8-node quadrilateral element, (c) 9-node crack-tip element, and (d) special 9-node quadrilateral element

An example of a mesh for the CT specimen of a particular thickness $t/a = 1$ is shown in Figure 3.4. By exploiting the symmetry of its geometry, the mesh generation effort can be significantly reduced. For instance, only one of the top and bottom surfaces, one of the two holes, one half of the two side-faces, and one half of the crack surface are required to be meshed. Meshes for the remaining boundary and crack surface can simply be obtained by the reflection about a plane of symmetry. It is evident also that only a region on the crack surface close to the crack front (see Figure 3.4(b)) and a region on the two side-faces surrounding the vertices (see Figure 3.4(c)) have a relatively finer mesh when compared with the other regions. Most of the effort and care is therefore spent to achieve a good mesh in such region and the corresponding transition zone. A good quality mesh with sufficient refinement is anticipated to yield accurate stress intensity factors along the entire crack front.

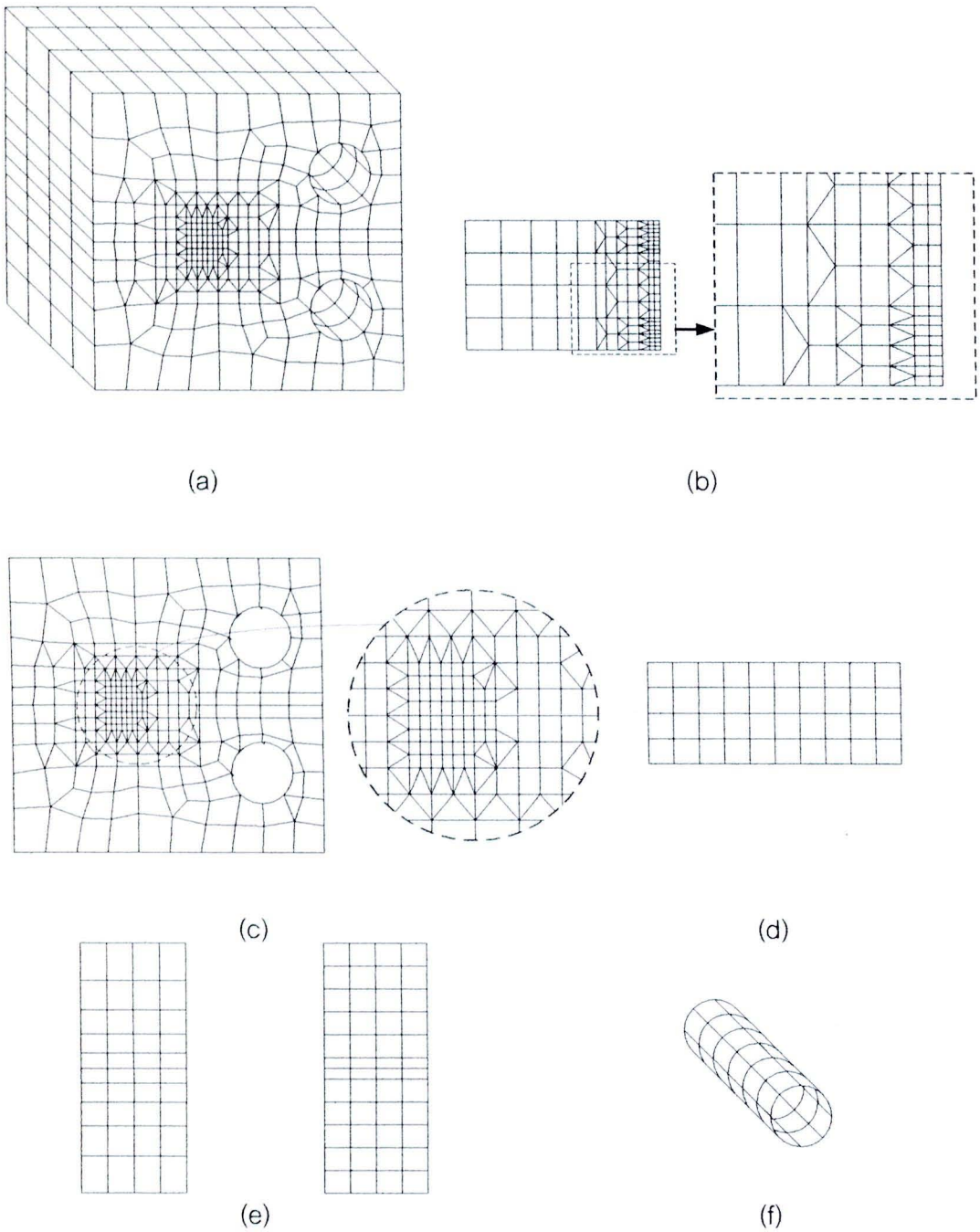

Figure 3.4 Example of mesh for CT specimen of thickness $t/a = 1$: (a) mesh for entire specimen, (b) mesh for crack surface, (c) mesh for side faces, (d) mesh for top and bottom surfaces, (e) mesh for back and front faces, and (f) mesh for holes

3.5 Convergence study

The main focus of this section is to explore the convergence of the stress intensity factor along the crack front using a series of meshes with different levels of

refinement. Results from this convergence study are very useful in the selection of a mesh that yields accurate numerical solutions while requiring relatively cheap computational cost.

In the study, three meshes, a coarse mesh denoted by Mesh-1, a medium mesh denoted by Mesh-2 and a fine mesh denoted by Mesh-3, are constructed as shown in Figures 3.5-3.7 for a specimen of thickness $t/a = 1$. The number of nodes and elements on the crack surface and the remaining boundary for the three meshes is reported in Table 3.1. In the analysis, we consider three different materials, one associated with an isotropic material with Poisson's ratio $\nu = 0.30$ and the other two corresponding to the transversely isotropic material with elastic constants chosen to be those for zinc and cadmium as given in Table 3.2. It should be noted that for the last two materials, the axis of material symmetry is chosen to direct perpendicular to the crack surface.

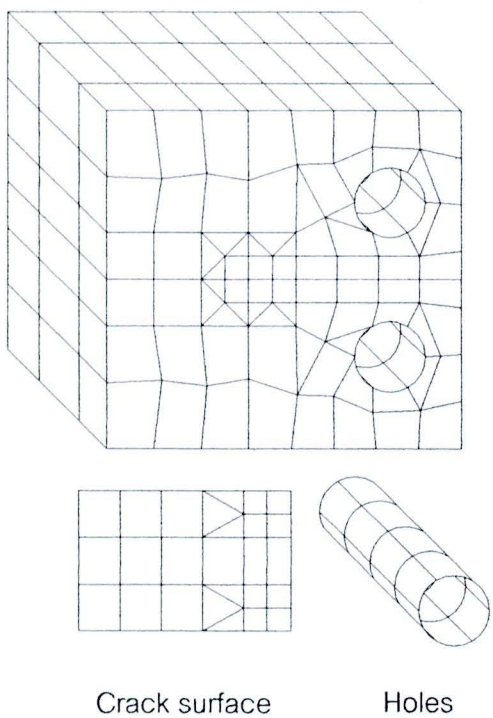

Figure 3.5 Coarse mesh or Mesh-1 for CT specimen thickness $t/a = 1$

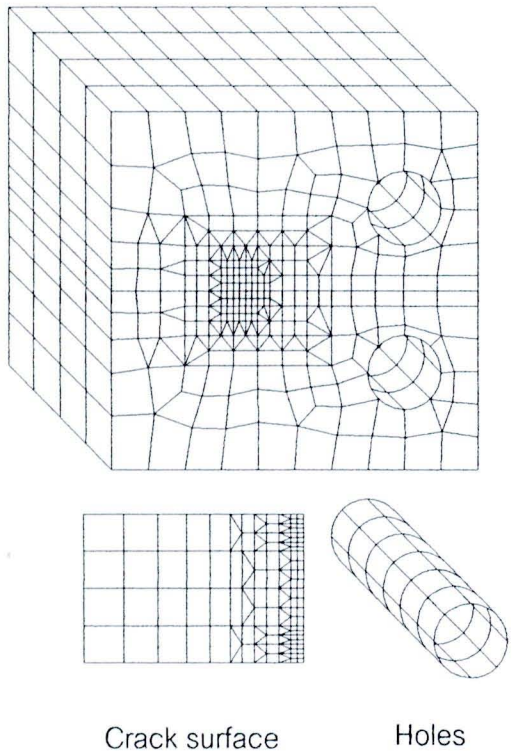

Figure 3.6 Medium mesh or Mesh-2 for CT specimen thickness $t/a=1$

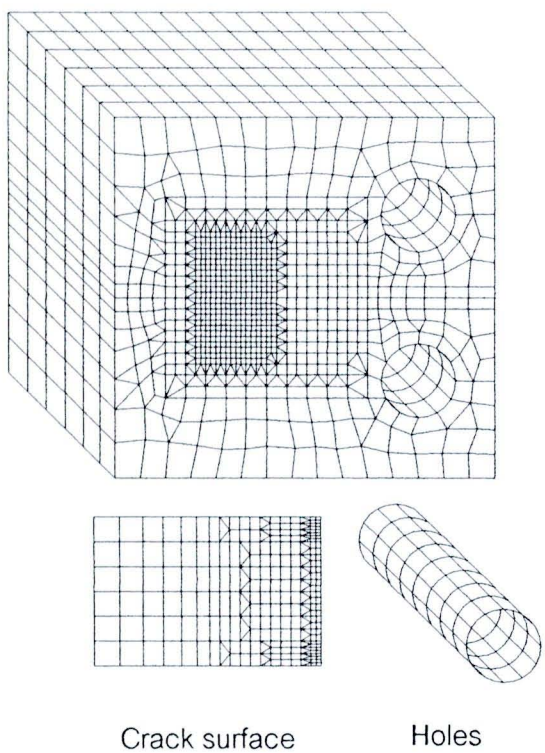

Figure 3.7 Fine mesh or Mesh-3 for CT specimen thickness $t/a=1$

Table 3.1 Number of nodes and elements for three meshes shown in Figures 3.5-3.7

Mesh	Number of nodes			Number of elements		
	Total	Boundary	Crack	Total	Boundary	Crack
1	927	829	98	324	298	26
2	2892	2425	467	1050	900	150
3	7614	6781	833	2704	2436	268

Table 3.2 Elastic constants (GPa) for zinc and cadmium (e.g. Freund and Suresh, 2003). The axis of material symmetry is taken to direct along the x_3-coordinate direction.

Materials	E_{1111}	E_{1122}	E_{1133}	E_{3333}	E_{1313}
Zinc	161	34.2	50.1	61	38.3
Cadmium	115.8	39.8	40.6	51.4	20.4

Numerical results for the mode-I stress intensity factor along the crack front are reported for three materials and three meshes in Figure 3.8. It is evident that results obtained from the Mesh-2 and Mesh-3 are almost identical while those from the Mesh-1 exhibit slight difference especially very near the vertices where the stress intensity factor drops very rapidly. This should imply the rapid convergence and the weak dependency on the level of mesh refinement for both isotropic and anisotropic cases. Next, we investigate the convergence behavior of numerical results for the same specimen but with the thickness $t/a = 4$. Meshes used in the analysis for this particular case are obtained by simply scaling coordinates in the direction along the thickness of the three meshes shown in Figures 3.5-3.7. Again, results of the mode-I stress intensity

factor (see Figure 3.9) lead to the same conclusion as the previous case and, in particular, stretching meshes in the thickness direction by four times still does not alter the convergence characteristic of the numerical solutions. It is worth noting that approximate solutions of this high quality can be achieved via the use of relatively coarse meshes due mainly to the application of special crack-tip elements along the crack front.

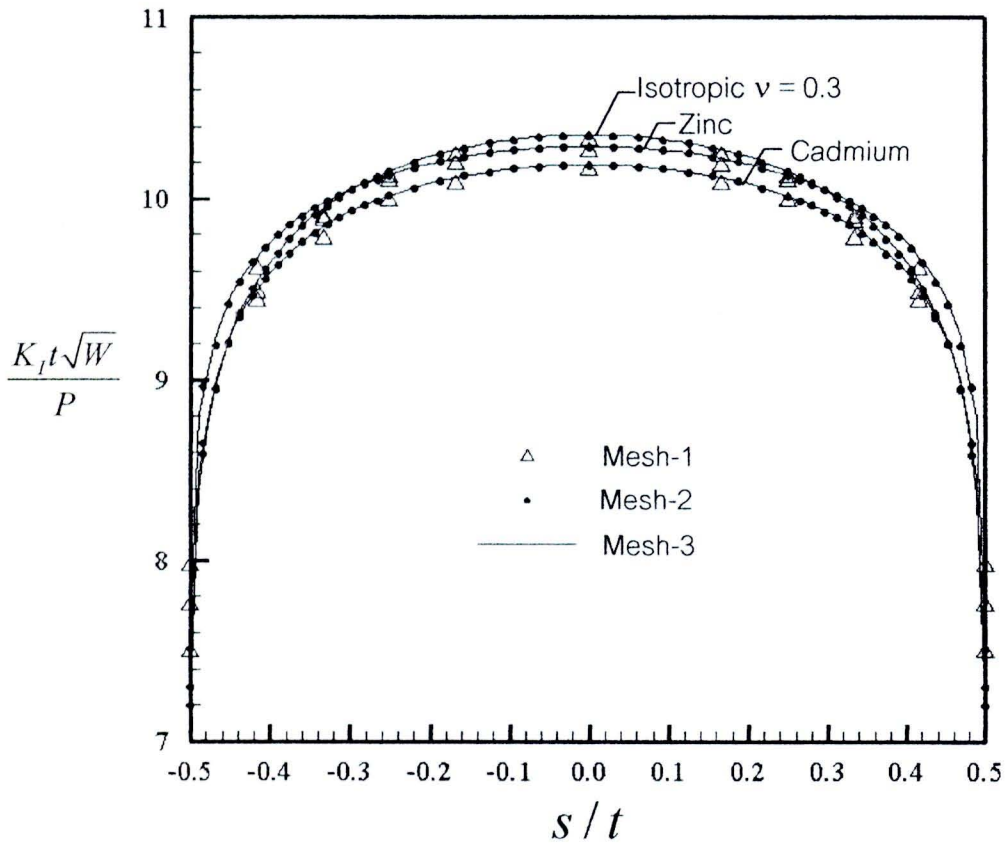

Figure 3.8 Normalized mode-I stress intensity factor along the crack front for CT specimen thickness $t/a = 1$. Results are reported for three meshes and three materials and S denotes the distance measured from the center of the crack front.

Since the medium mesh and the fine mesh yields results of comparable accuracy while the latter consumes substantially more computational time, a level of refinement similar to that for the former mesh will be used in the construction of meshes

for a CT specimen of other thicknesses in the parametric study to explore the behavior of the stress intensity factor along the entire crack front.

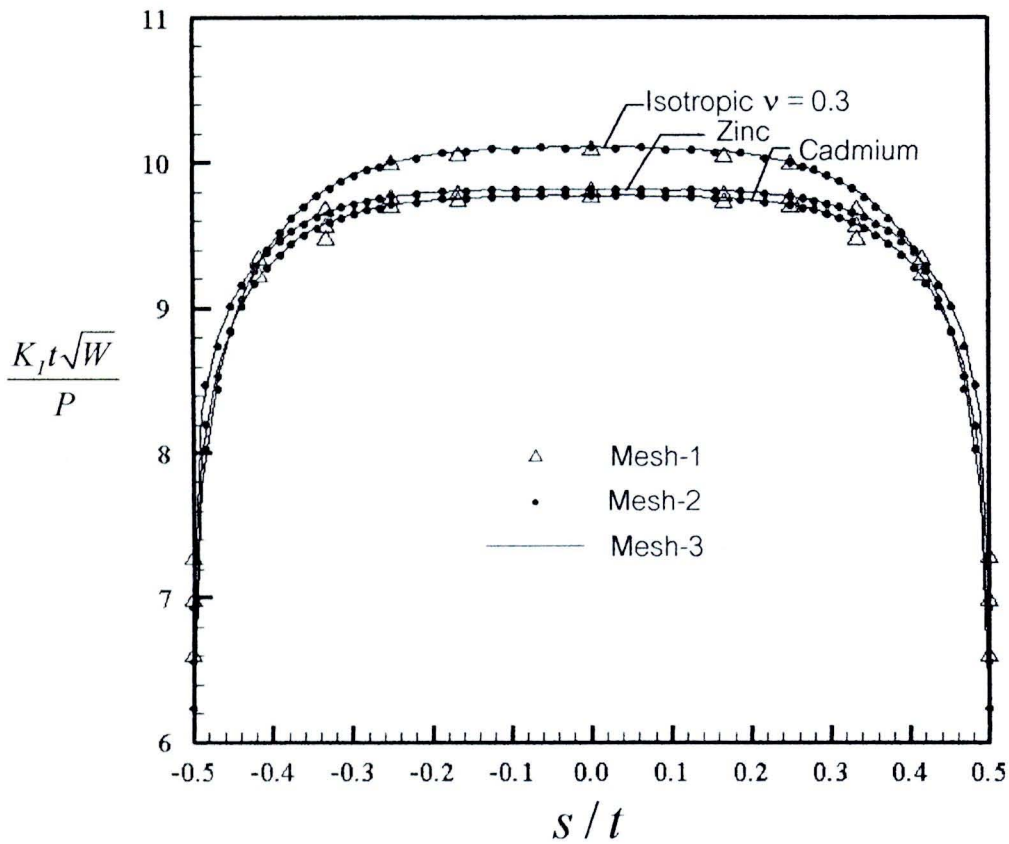

Figure 3.9 Normalized mode-I stress intensity factor along the crack front for CT specimen thickness $t/a = 4$. Results are reported for three meshes and three materials and S denotes the distance measured from the center of the crack front.

3.6 Verification of numerical results

To verify the numerical results obtained from the weakly singular SGBEM, comparisons with existing benchmark solutions for a two-dimensional plane strain case and for isotropic materials are performed. Consider a CT specimen of sufficiently large thickness to ensure the existence of a plane strain condition in the central region of the crack front. Numerical results obtained from a mesh with the same level of refinement as the medium mesh shown in Figure 3.6 are reported along with the plane strain solution proposed by ASTM E399-90 (1997) in Figure 3.10 for Poisson ratio

$\nu = 0.1$ and in Figure 3.11 for Poisson ratio $\nu = 0.3$. It is evident that the SGBEM solutions (in the region exhibiting the plane strain condition) show very good agreement with the benchmark solution. Besides this verification, it should be noted that extensive verification of the weakly singular SGBEM and its formulation used in the present study was already performed by Li *et al.* (1998), Rungamornrat (2006), and Rungamornrat and Mear (2008b) for various crack problems associated with both isotropic and transversely isotropic media.

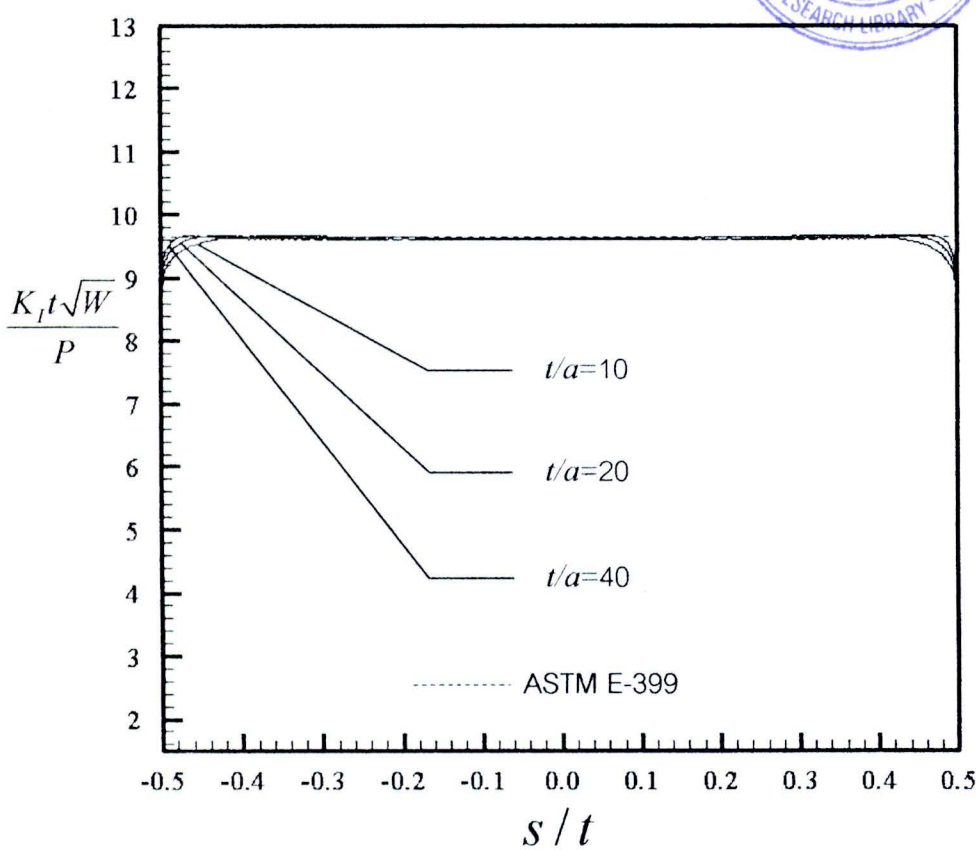

Figure 3.10 Normalized mode-I stress intensity factor along the crack front for CT specimen for sufficiently large thicknesses along with the plane strain solution from ASTM E399-90 (1997). Results are reported for isotropic material with $\nu = 0.1$ and s denotes the distance measured from the center of the crack front.

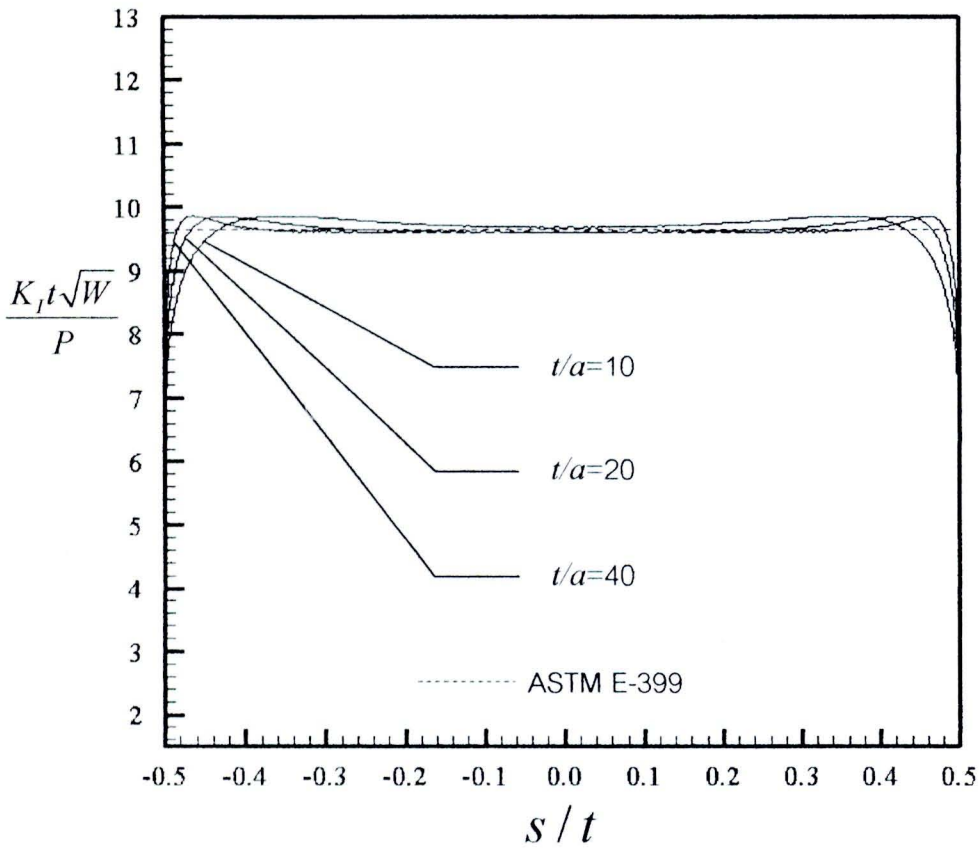

Figure 3.11 Normalized mode-I stress intensity factor along the crack front for CT specimen for sufficiently large thicknesses along with the plane strain solution from ASTM E399-90 (1997). Results are reported for isotropic material with $\nu = 0.3$ and s denotes the distance measured from the center of the crack front.

3.7 Mesh for CT specimen with different thickness

To construct meshes for the CT specimen of various thicknesses, the medium mesh for $t/a = 1$ shown in Figure 3.6 is used as a prototype. Two following simple strategies, (i) mesh stretching along the crack front direction and (ii) adding an inner layer, are employed. The mesh stretching is applied first to obtain a series of meshes for several thicknesses without adding nodes and elements but simply scaling the coordinate along the crack front. However, this strategy can be used up to a certain thickness in order to avoid elements of large aspect ratios and produce too coarse

meshes. For a specimen with too large thickness to use the first strategy, the second strategy is employed instead by adding a layer of elements and nodes in the central region of the crack front. With this particular means, the mesh for the two side-faces does not alter. With the proper combination of these two schemes, a series of meshes can be constructed for the CT specimen of thickness ranging from $t/a = 1$ to $t/a = 40$. Examples of meshes for CT specimen of certain thicknesses are shown in Figures 3.12-3.13.

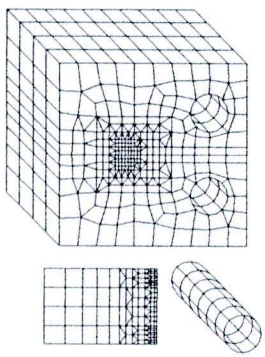

(a)

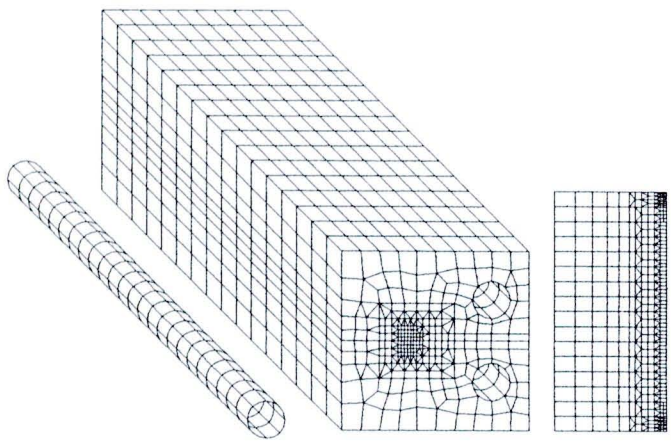

(b)

Figure 3.12 Meshes for CT specimen: (a) $t/a = 1$ and (b) $t/a = 5$

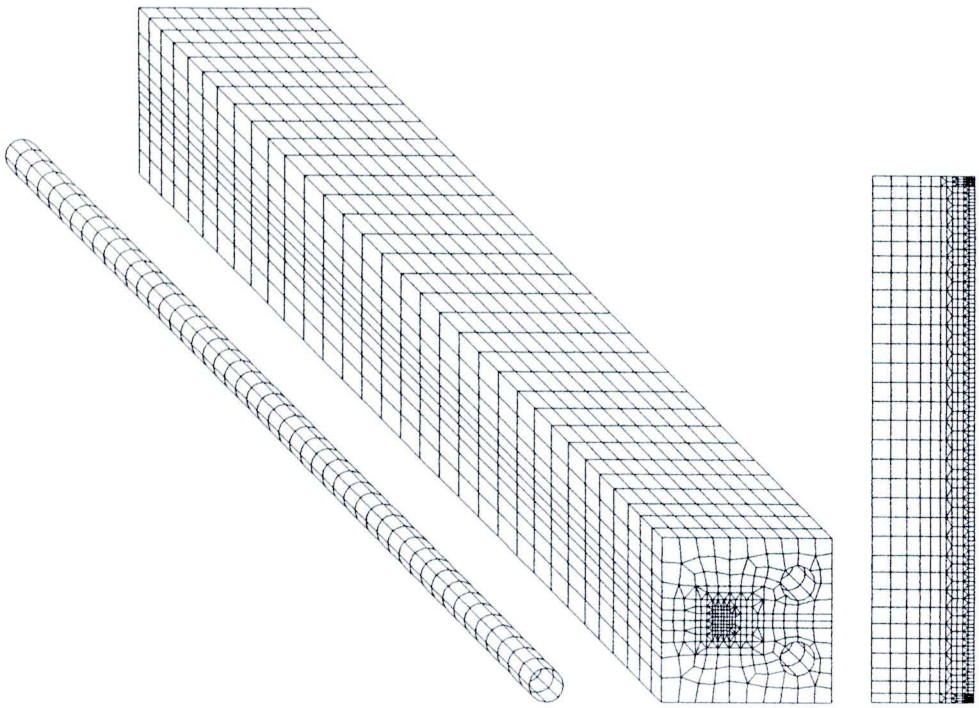

Figure 3.13 Mesh for CT specimen for $t / a = 10$